Mineralogical Magazine, October 2000, Vol. 64(5), pp. 945–959

Three-dimensional study on the interconnection and shape of crystals in a graphic granite by X-ray CT and image analysis

S. IKEDA[1,*,†], T. NAKANO[2] AND Y. NAKASHIMA[3]

[1] Geological Institute, Graduate School of Science, University of Tokyo, Hongo, Bunkyo-ku, Tokyo 113-0033, Japan
[2] Geological Information Centre, Geological Survey of Japan, Higashi, 1-1-3, Tsukuba, Ibaraki 305-8567, Japan
[3] Geophysics Department, Geological Survey of Japan, Higashi, 1-1-3, Tsukuba, Ibaraki 305-8567, Japan

ABSTRACT

The technique of investigating 3-dimensional interconnections and the shapes of crystals in a rock by X-ray computerized tomography (CT) and image analysis was developed using a graphic granite specimen as an example. Fifty 2-dimensional tomographic images (slices) of the graphic granite were obtained 'non-destructively' using a medical X-ray CT scanner. Since a CT value of the specimen was decreased with increasing cross-sectional sample area by the effect of beam-hardening, the CT value was corrected using the area of each slice. Binary images of the slices were made comparing one of them with a thin-section of the slice. Using the binary images, connection analysis of quartz rods in the graphic granite specimen was performed on the basis of percolation theory (cluster labelling). This analysis showed that at least 89.9% of the quartz rods were connected in three dimensions. Furthermore, the 3-dimensional shape of the quartz rods was analysed using the 2-point correlation function calculated from the binary images. The average shape of the quartz rods was obtained by fitting an ellipsoid to the high-value region of the 2-point correlation function. The elongation axis of the ellipsoid agreed well with the crystallographic *c*-axes of the quartz rods.

KEYWORDS: X-ray CT, 3-dimensional image analysis, graphic granite, cluster labelling, 2-point correlation function.

Introduction

IN the Earth Sciences, textures in rocks are examined in two dimensions using thin-sections or polished sections. Sometimes, 2-dimensional investigation is enough to quantify 3-dimensional characteristics of texture. For example, if an appropriate model of crystal shape is assumed, we can determine a 3-dimensional crystal size distribution from a 2-dimensional distribution by stereology (e.g. Cashman and Marsh, 1988). However, many features of the 3-dimensional structure cannot be investigated by 2-dimensional observation. A 3-dimensional network structure, such as a pore network, is often interpreted as separate pores by 2-dimensional observation. Also, interconnection of crystals in three dimensions cannot be recognized by 2-dimensional analysis. The interconnections of crystals contain significant information relating to the origins of the rocks, e.g. the process of magma differentiation (Philpotts *et al.*, 1998). Therefore, it is important to develop the technique to analyse a 3-dimensional network structure.

There are some techniques to investigate the 3-dimensional internal structure of rocks. For example, Bryon *et al.* (1995), Cooper and Hunter (1995) and Marschallinger (1998) demonstrated 3-dimensional reconstructions of the internal structures in rock samples using successive digitized images acquired by serial thin-sectioning or lapping. Philpotts *et al.* (1998)

* E-mail: ikeda@chem.s.u-tokyo.ac.jp
† Present address: Department of Complexity Science and Engineering, Graduate School of Frontier Sciences, University of Tokyo

discovered the 3-dimensional network structure (chains) of plagioclase phenocrysts in a basalt specimen by a partial melting experiment. However, the technique of serial polishing needs skill and time. Also, the techniques of partial melting or selective dissolution with acids or alkalis are not appropriate for every sample.

Nowadays, we can observe the internal structures of rocks by non-destructive methods, such as X-ray computerized tomography (CT). X-ray CT was invented and developed in the medical field in the 1970s and has been applied to geological samples in recent years. For example, by the X-ray CT method, we can analyse directly the 3-dimensional crystal-size distribution, crystal spatial disposition (Denison *et al.*, 1997; Denison and Carlson, 1997), and structure of cracks or pores (Raynaud *et al.*, 1989; Nakano *et al.*, 1992; Nakashima *et al.*, 1997). However, the techniques to investigate the 3-dimensional connection and shape of crystals have not become well established. Furthermore, X-ray CT images generally have an error resulting from beam-hardening (see below). This error affects precise analysis. In this study we developed a technique to correct the error and to investigate the 3-dimensional connection and shape of crystals in a rock by combining the X-ray CT method and image analysis. The connection analysis was based on the technique of pore-network analysis proposed by Nakano *et al.* (1992). Graphic granite was selected as an example for these analyses because quartz rods in graphic granite are known to connect to each other as illustrated in the following section.

Specimen and interconnection of quartz rods

We used the specimen of graphic granite shown in Fig. 1 (Sample GSJ-R6052, from the Geological Survey of Japan). This specimen was obtained by H. Matsubara (Matsubara, 1956) from the Shiozawa district in Ishikawa town, Fukushima Prefecture, Japan. Around Ishikawa, there are many granitic pegmatites within a granitic body intruded into the Abukuma metamorphic belt. The specimen was collected from a graphic granite layer in one of the pegmatite bodies (Matsubara, 1956). The K-Ar age of the surrounding granitic body is 90–100 m.y. (Kawano and Ueda, 1967).

The specimen consists of quartz rods and host alkali-feldspar (microcline microperthite). In the specimen, most of the quartz rods show

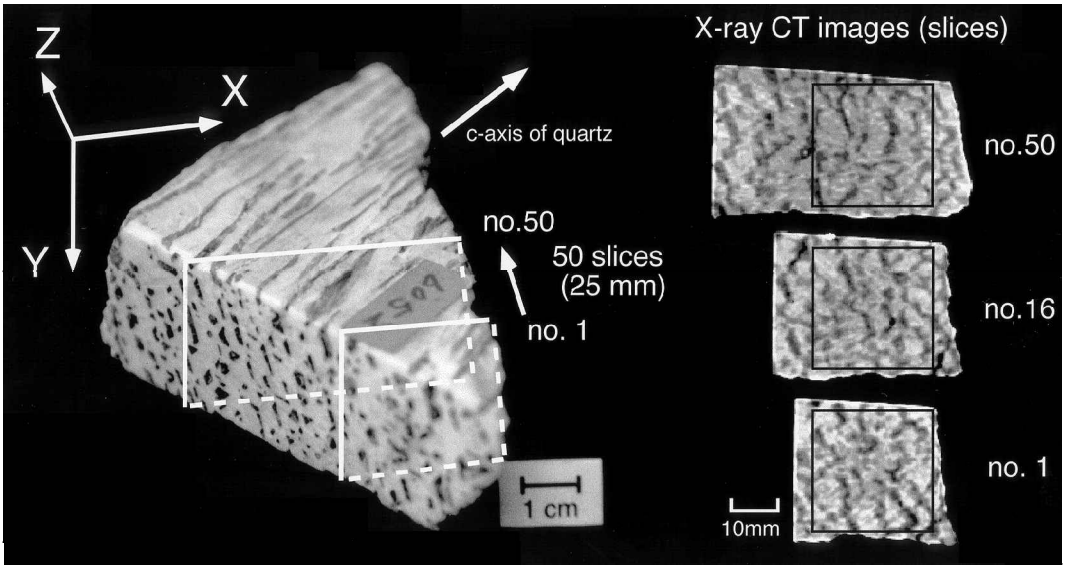

FIG. 1. Specimen of graphic granite (GSJ-R6052) with coordinate system for the X-ray CT (left), and three slices (right). Fifty slices parallel to the *XY*-plane were obtained along the *Z*-axis. The dark parts are quartz rods both in the photograph of the specimen and in the CT images. The areas surrounded by black lines in the CT images were used for the three-dimensional analysis and correspond to the areas of images shown in Fig. 4.

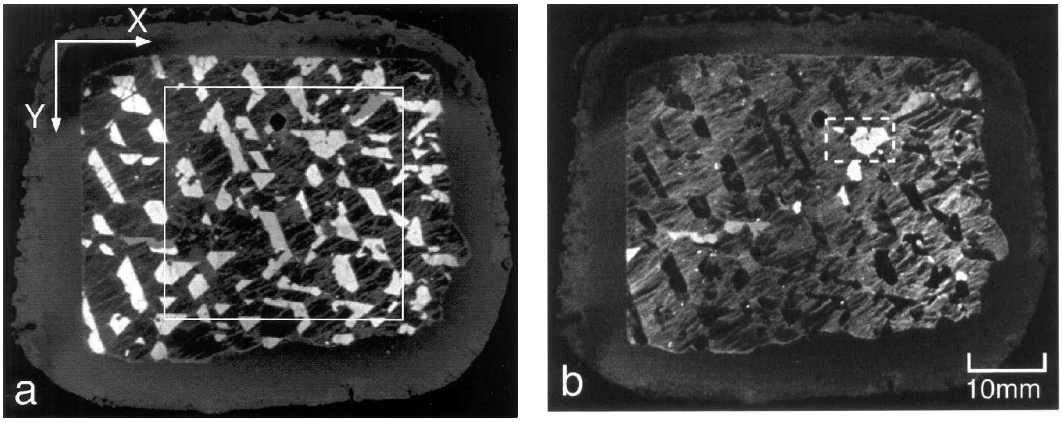

FIG. 2. Photographs of the thin-section of the X-ray CT image no. 16. in crossed polars. (*a*) Simultaneous extinction of alkali feldspar host. The bright parts are quartz grains. (*b*) Simultaneous extinction of most of the quartz rods. The quartz rod surrounded by the broken line has three domains with different crystallographic orientations. The dark domain in the rod shows the simultaneous extinction with most of the quartz rods. The dark circular region near the corner of the box (broken line) was lost in the process of making the thin-section.

simultaneous extinction (Fig. 2) as reported in many previous studies (e.g. Wahlstrom, 1939; Simpson, 1962). Furthermore, we confirmed, using a precession camera, that the elongation direction of the quartz rods correspond approximately with the crystallographic *c*-axis of quartz. In order to find the cause of the simultaneous extinction, Simpson (1962) performed successive surface grinding of a graphic granite specimen and showed interconnections of the quartz rods. He concluded that the simultaneous extinction occurs because all quartz rods are parts of the same crystal. Therefore, we concluded that graphic granite was a good choice of material to investigate 3-dimensional crystal interconnection.

X-ray CT

X-ray CT is a non-destructive technique used to determine tomographic maps of the X-ray linear attenuation coefficient in an object. We describe the 2-dimensional X-ray CT images as 'slices'. The brightness in the slices (e.g. in Fig. 1) shows the linear attenuation coefficient, which depends on the density and chemical composition of the object and the energy of the incident X-ray beam (Koch and MacGillavry, 1962; McCullough, 1975; Denison *et al.*, 1997).

The linear attenuation coefficient obtained by X-ray CT is generally called the 'CT value'. It is a dimensionless number normalized by the linear attenuation coefficient of water as defined by the following equation

$$\text{CT value} = \frac{\mu - \mu_w}{\mu_w} \times 1000 \qquad (1)$$

where μ and μ_w are the linear attenuation coefficients of the object and water, respectively.

We used a medical X-ray CT scanner (Hitachi CT-W2000) to obtain the slices of the specimen. The scanner belongs to the third-generation type adopting a continuous rotation method. The continuous (polychromatic) X-ray beam from a target of Mo-W alloy was used. The voltage and current of the X-ray tube were 120 kV and 175 mA respectively. The X-ray exposure time for each slice was 4.0 s. We used the 3-dimensional coordinate system for acquisition of the X-ray CT images shown in Fig. 1 (*XYZ*-axes). The slices lay in the *XY*-plane. The size of the voxel (volume element in three dimensions; corresponding to 'pixel' in two dimensions) on the *XY*-plane was 0.313×0.313 mm^2, which was considered as the in-plane resolution in the slices. The thickness of each slice was 1.0 mm. The specimen was automatically moved along the *Z*-axis by 0.5 mm after acquisition of each slice. Thus each slice overlaps by 0.5 mm in thickness with the adjacent slices. Fifty 16-bit images (slices) along the *Z*-axis were obtained in all. It took 28 min to acquire 50 slices.

With the graphic granite specimen, the CT value of alkali feldspar (~2080) was greater than that of quartz (~1980), though the density of alkali feldspar is lower than that of quartz. The higher CT value of alkali-feldspar depends on high attenuation by K (Raynaud *et al.*, 1989). As described above, the linear attenuation coefficient is a function not only of density but also of chemical composition and the energy distribution of the X-ray beam. We confirmed the attenuation coefficients of alkali feldspar and quartz using the formulae and attenuation coefficients of McCullough (1975) and Hubbell *et al.* (1980) at an X-ray energy of <120 keV.

Image analysis techniques

Correction of beam-hardening

The CT value obtained using a continuous (polychromatic) X-ray beam is influenced by the beam-hardening (Denison *et al.*, 1997). The low-energy component of X-ray photons is more absorbent than the high-energy component. Thus, most of the low-energy photons are absorbed at the periphery of a specimen just after entry of the X-ray beam into the specimen. In the X-ray CT technique, image reconstruction is performed using the sum total of the photons belonging to all energy levels as intensity data; thus the linear attenuation coefficient at the periphery, where many photons are absorbed, is calculated as a high value even if the specimen is homogeneous. This beam-hardening causes two types of errors in the CT value. One error arises from the heterogeneity of the CT value within each slice. The CT value at the centre of the slice is lower than that at the periphery even in the homogeneous material. The heterogeneity within each slice was not seriously affected by omitting the periphery from the analysed area (Fig. 1 right). The other error is the difference in the CT value between different slices. A slice with large cross-section area (e.g. no. 50 in Fig. 1) has a lower CT value than a slice with small area (e.g. no. 1 in Fig. 1). In this study, the difference in the CT values amongst the slices was very large, and we had to correct for it. As shown in detail later, we found a simple relationship between the error (difference of CT value) and the cross-sectional area of the slice. The increase of the CT value was proportional to the decrease of the area of the slice. We corrected the CT value of each slice in proportion to the decrease of the area.

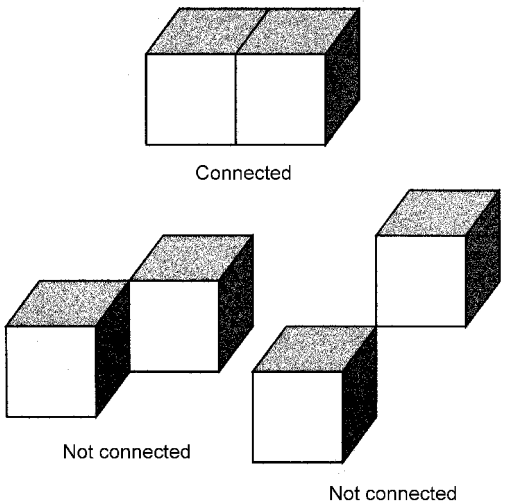

FIG. 3. Definition of connection of voxels occupied by quartz crystal in the three-dimensional image.

Thresholding

In order to perform 3-dimensional analysis, we made binary images of the fifty slices using an ordinary thresholding (segmentation) technique of a grey level image (e.g. Dilks and Graham, 1985), and identified the quartz rods as follows. Firstly, the binary image of slice no. 16 was made by comparing it carefully with the thin-section corresponding to the slice (Fig. 2). Since the CT value at the edge of the specimen becomes much larger owing to the effect of the beam-hardening (and because of the Gibbs' phenomenon relating to the algorithm of image reconstruction) as described above, we cut out an area of 28×28 mm^2 (90×90 voxels) from the original slice and used it for the 3-dimensional analysis. Binary images of the other 49 slices were made in the same way. The cut-out areas on several slices are shown in Fig. 1 (right).

Connection analysis (Cluster labelling)

We developed software to visualize and analyse objects from 3-dimensional X-ray CT images (Nakano and Fujii, 1989*a*, 1991; Nakano *et al.*, 1992, 1997). The binary images were used to analyse the connection of quartz rods. In percolation theory, the analysis is known as the 'cluster labelling method' (Stauffer, 1985). In this analysis, connection of two adjacent voxels in the

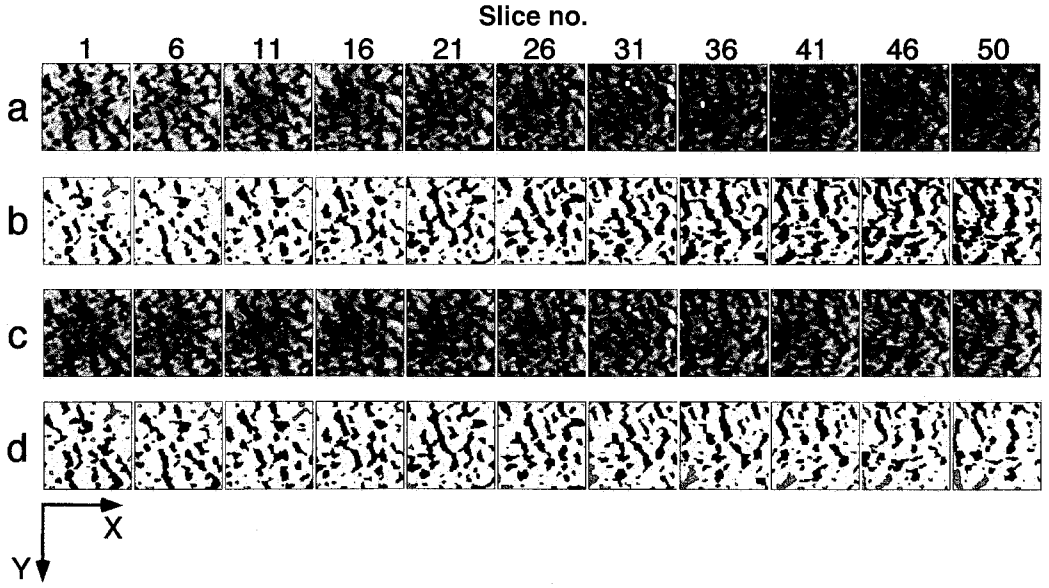

FIG. 4. Grey level images and binary images before and after the correction of CT value. Only 11 of 50 slices are shown (every 5 slices). Each image consists of $90 \times 90 = 8100$ voxels (28×28 mm^2). (*a*) 16-bit grey level images before the correction. (*b*) Binary image before the correction. (*c*) 16-bit grey level images after the correction. (*d*) Binary image after the correction. In the binary images, the black region indicates the quartz rods which belong to the largest cluster while the grey indicates the quartz rods which do not belong to the largest cluster in Fig. 6*f*.

quartz rods is evaluated as shown in Fig. 3. When two voxels shared a face, we considered them as connecting voxels. When two voxels contacted only at a vertex or an edge, we considered them as separate voxels. This criterion is commonly used in the connectivity analysis (Stauffer, 1985; Nakano and Fujii, 1989*b*). We call connected voxels a 'cluster'. The extent of interconnection of quartz rods was assessed quantitatively using the term 'connectivity' which is a volume fraction relating the largest cluster of quartz rods to the volume of all quartz rods (Nakano and Fujii, 1989*b*):

$$\text{Connectivity} = \frac{\text{Volume of the largest cluster}}{\text{Total volume of all quartz rods}} \quad (2)$$

From this definition, the connectivity becomes 1 when all quartz rods are connecting in the specimen.

Shape analysis

In order to analyse the 3-dimensional shape of quartz rods, a 2-point correlation function (e.g. Berryman, 1985; Berryman and Blair, 1986) was calculated in three dimensions. The 2-point correlation function represents two significant spatial correlation features. One is the long-distance correlation such as the spatial distribution of minerals in rocks (Morishita and Obata, 1995; Morishita, 1998). In this case, we can obtain information on the degree of randomness for individual minerals, the mean distance between different minerals, etc. The other feature of the function is the short-distance correlation about the origin, and it represents the average shape of an object. We used the latter feature of the function. In the graphic granite specimen shown in Fig. 1, the quartz rods seem to extend (grow) in the same direction; thus it was expected that the 2-point correlation function of the quartz rods would show meaningful results with respect to their average shape. Furthermore, it is known that the 2-point correlation function is not strongly influenced by the noise of the image data; thus it was expected that we could perform precise shape analysis.

In binary images, each voxel has a value of 1 or 0. Here we define the value of each voxel $B(\mathbf{r})$ in the $\mathbf{r}$ space as follows:

$$B(\mathbf{r}) = \begin{cases} 1 & \text{when the voxel was in the quartz rods} \\ 0 & \text{when the voxel was not in the quartz rods} \end{cases}$$

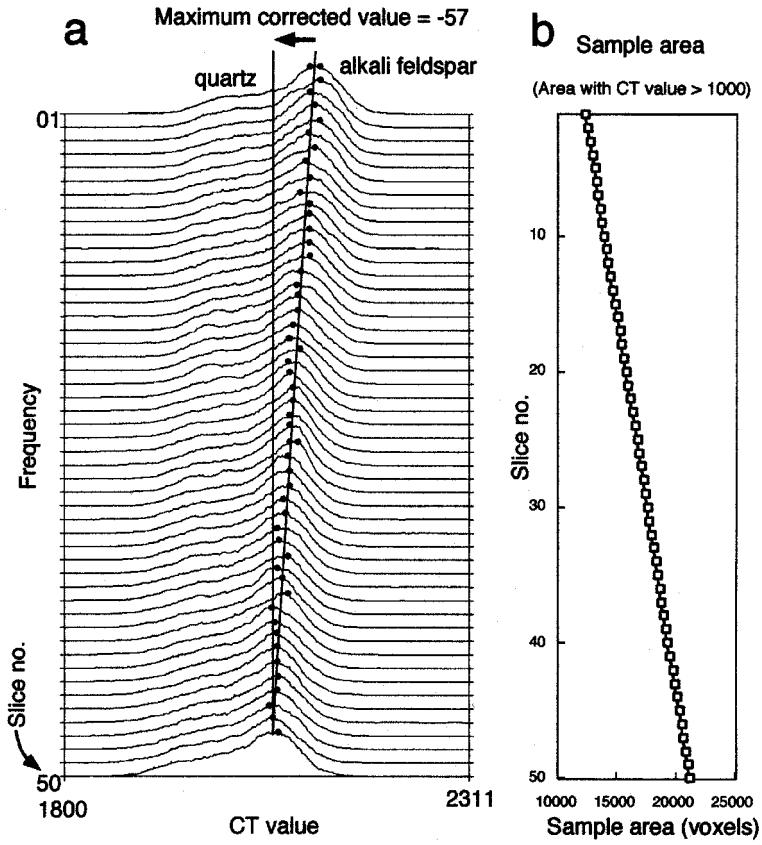

FIG. 5. (*a*) Histograms of the CT value for 50 slices (grey level) of 16-bit CT images shown in Fig. 4*a* (before the CT value correction). The horizontal axis indicates the CT value. The vertical axis indicates the frequency of the voxels. The solid circle on each histogram indicates the peak level of alkali feldspar. (*b*) Variation of cross-sectional area of the specimen with slice no. The areas correspond to the number of voxels with CT value >1000.

The 2-point correlation function of quartz is expressed as

$$AC(\vec{\delta}) = \langle B(\vec{r}) \cdot B(\vec{r}+\vec{\delta})\rangle_{\vec{r}} \qquad (4)$$

where the brackets $\langle\ \rangle_{\vec{r}}$ indicate a volume average over the spatial coordinate $\vec{r}$. In three dimensions, $AC(\vec{\delta})$ is written as $AC(dx, dy, dz)$. $AC(0,0,0)$, which is the value at the origin, shows the highest value and represents the volume fraction of the object (i.e. the quartz rods). Around the origin, there is a spatial field having high $AC(dx, dy, dz)$ values, and the field is considered to represent the average shape of the objects. In this study, an ellipsoid was fitted to the field whose $AC(dx, dy, dz)$ values were greater than or equal to half of $AC(0,0,0)$ using the method shown in the Appendix.

Results and discussion

Data correction and thresholding

Three slices of a 2-dimensional X-ray CT image are shown in Fig. 1 (right). As described above, there was a large difference in the CT value between the slices. Figure 4*a* shows the 11 slices (every 5 slices) of grey-scale images (90×90 voxels) before the CT value correction. If we carry out thresholding with a fixed threshold value (grey level), we obtain the binary images shown in Fig. 4*b*. The slices having a larger slice number show a higher volume fraction of quartz rods.

This trend is not consistent with what we see in thin-sections. From our observations of several thin-sections, the volume fraction of quartz rods in the specimen is almost the same from slice no. 1 to no. 50. Figure 5*a* shows histograms of the CT value for all slices. The solid circle at the top of the each histogram indicates the CT value of alkali feldspar. We recognize the systematic shift in peak position of alkali feldspar. Figure 5*b* shows the variation of the cross-sectional area of the slices. The areas of the slices increase with increasing slice number. Since the variation of the area is almost linear with the slice no. (Fig. 5*b*), we considered that the linear shift in the peak position of the histogram (Fig. 5*a*) was caused by the beam-hardening, depending on the variation of the cross-sectional sample area. Thus we corrected the CT value of all slices by shifting the histograms as shown in Fig. 5*a*, on the assumption that the peak position of alkali-feldspar must be the same in all slices. The corrected (shift) value of each slice was determined as (maximum corrected value) × (50 – slice no.)/49.

The corrected grey level images are shown in Fig. 4*c* and the binary images obtained by the thresholding are shown in Fig. 4*d*. The threshold CT value extracting only quartz (2024) was determined by comparing slice no. 16 with its thin-section. After the data correction, the area of the quartz rods become almost the same for all slices (Fig. 4*d*).

Connection analysis (cluster labelling)

Figure 6 shows the result of the 3-dimensional connection analysis (cluster labelling) using the binary images. The sub-figures show a bird's-eye view reconstructed using: (*a*) 1 slice; (*b*) 5 slices; (*c*) 10 slices; (*d*) 20 slices; (*e*) 30 slices; and (*f*) 50 slices, respectively. The left column of this figure shows all the quartz rods and the right column shows only the largest cluster of connected quartz rods. The sub-figures in the right column (*a*–*f*) indicate the results of connection analysis calculated individually using the data from 1, 5, 10, 20, 30 and 50 slices, respectively. Results (*a*–*e*) are not part of result *f* analysed using 50 slices. We have defined the 'connectivity' in equation 2 as the volume fraction of the largest cluster of the quartz rods (Fig. 6, right) to all quartz rods (Fig. 6, left). The calculated connectivities were (*a*) 0.133, (*b*) 0.160, (*c*) 0.337, (*d*) 0.379, (*e*) 0.794 and (*f*) 0.899, respectively. With up to five slices (Fig. 6*b*; 2.5 mm in the *Z*-direction), connectivity did not increase.

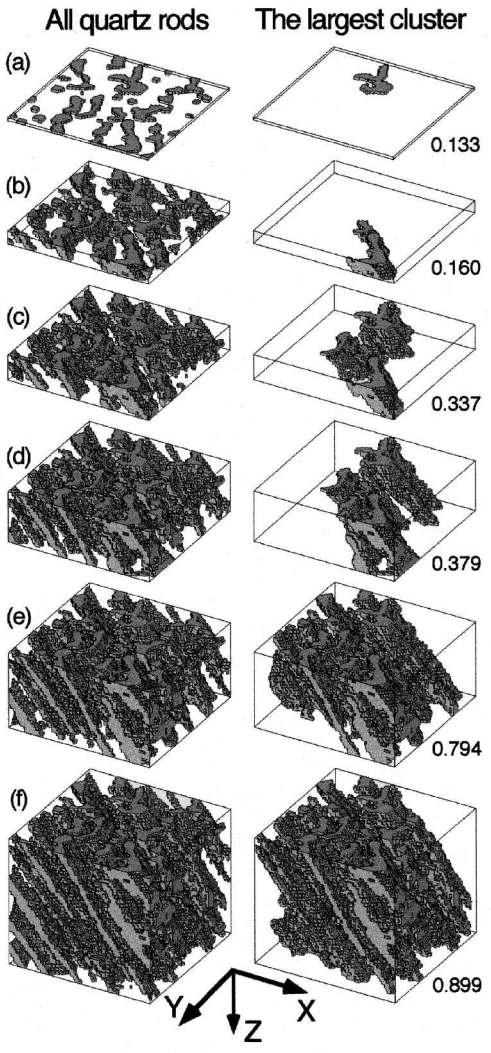

FIG. 6. 'Bird's eye view' representing 3-dimensional connection analysis (cluster labelling) of quartz rods. The left column shows all the quartz rods in the analysed area while only the largest cluster of quartz rods is shown in the right column. Each figure shows the image constructed using slices of (*a*) no. 1, (*b*) no. 1–5, (*c*) no. 1–10, (*d*) no. 1–20, (*e*) no. 1–30 and (*f*) no. 1–50, respectively. Numerical values indicate the connectivity of quartz rods defined by equation 2. In (*a*–*f*), the top slice is the CT image no. 1. The *XYZ*-axes are identical to those of Fig. 1. The spatial extent of (*f*) is 28 mm (*X*) × 28 mm (*Y*) × 25 mm (*Z*).

Between (*b*) and (*c*), connectivity started to increase. With 50 slices (Fig. 6*f*; 25 mm in the *Z*-direction), almost all quartz rods (89.9%) were found to be connected. In Fig. 6*f*, the separate quartz rods (10.1%), which did not belong to the largest cluster, were located at the corners of the analysed space ($28 \times 28 \times 25$ mm^3). These separate rods are also shown in Fig. 4*d* in grey, and we can confirm that they are located at the corners. Thus, such quartz rods would be included in the largest cluster if the analysed space became larger. This result is consistent with the hypothesis of Simpson (1962) that all quartz rods are parts of the same crystal. By image analysis we were able to assess the interconnection quantitatively.

We could also investigate the structures of the junctions of connected quartz rods in *XZ*-planes synthesized by image processing (Fig. 7) though we could not clearly confirm those structures in XY-planes (X-ray CT images). Figure 7 shows how the quartz rods join or separate. Such information will be important in revealing the crystal growth mechanism of the quartz rods and the origin of graphic granite. These subjects (e.g. Fenn, 1986; Lentz and Fowler, 1992; Stel, 1992) will be discussed in a separate paper. By image analysis, we can obtain tomographic (2-dimensional) images of sections cut in any orientation and it becomes easy to investigate the structures. This is one of the significant points that advanced the technique compared to the serial surface grinding of Simpson (1962).

Thus, the combination of X-ray CT and 3-dimensional image analysis is a powerful tool in analysing the 3-dimensional interconnection of a mineral. However, we cannot identify the crystallographic orientation by these techniques. For example, even the quartz rods that did not show simultaneous extinction in Fig. 2*b* were also thought to be components of the largest cluster shown in Fig. 6*f*. However, this result is not a mistake of the above connection analysis. The quartz rod surrounded by the broken line in Fig. 2*b* consists of two domains some of which show simultaneous extinction with some of the quartz rods and some of which do not. Therefore, the quartz rods which do not show simultaneous extinction also touch the largest cluster, and the conclusion on the connection was true. The connectivity obtained by X-ray CT carries no information on the crystallographic orientations because the X-ray CT technique is not based on XRD but on X-ray absorption. Conversely, this aspect will be a good point to analyse the interconnection of poly-crystals having different crystallographic orientations, e.g. chains (network structure) of plagioclase phenocrysts in basalt discovered by Philpotts *et al.* (1998) in a partial melting experiment.

Shape analysis

We calculated a 2-point correlation function $AC(dx, dy, dz)$ using the binary images in order to analyse the 3-dimensional shape of the quartz rods (Fig. 8). The value at the origin $AC(0,0,0)$ was 0.232, which is the highest value and represents the volume fraction of quartz. In the $dz = 0$ slice, we can recognize the high $AC(dx, dy, dz)$ area around the origin (bright area). With decreasing dz, the area having the high AC value moves away from the centre point, and the AC value decreases gradually. Since the 2-point correlation function is symmetrical with respect to the origin $(dx, dy, dz) = (0,0,0)$, the bright area moves in the opposite direction in the slices for $+1 \leqslant dz \leqslant +10$, though these slices are not shown in Fig. 8. We carried out the ellipsoid fitting to the area with high correlation value $\geqslant 0.116$ (bold contours in Fig. 8), which was half of $AC(0,0,0)$. The fitting was performed by minimizing or maximizing the 2nd moments around the axes (Appendix).

The result of the ellipsoid fitting is shown in Fig. 9. The shape of the quartz rods could be approximated to an elongated ellipsoid with large aspect ratio. The elongation axis of the ellipsoid is considered to correspond with the elongation axes of the quartz rods with preferred orientation. This can be confirmed by comparing Figs 9 and 6*f*.

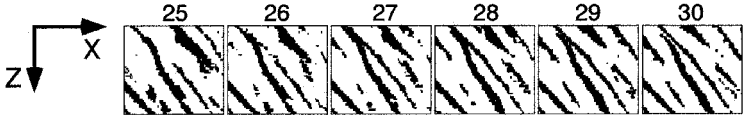

FIG. 7. Junctions of quartz rods recognized in binary images on the *XZ*-plane. The images were synthesized by a computer using 50 slices (*XY*-plane) obtained by X-ray CT. The numbers above the images indicate slice numbers along the *Y*-axis.

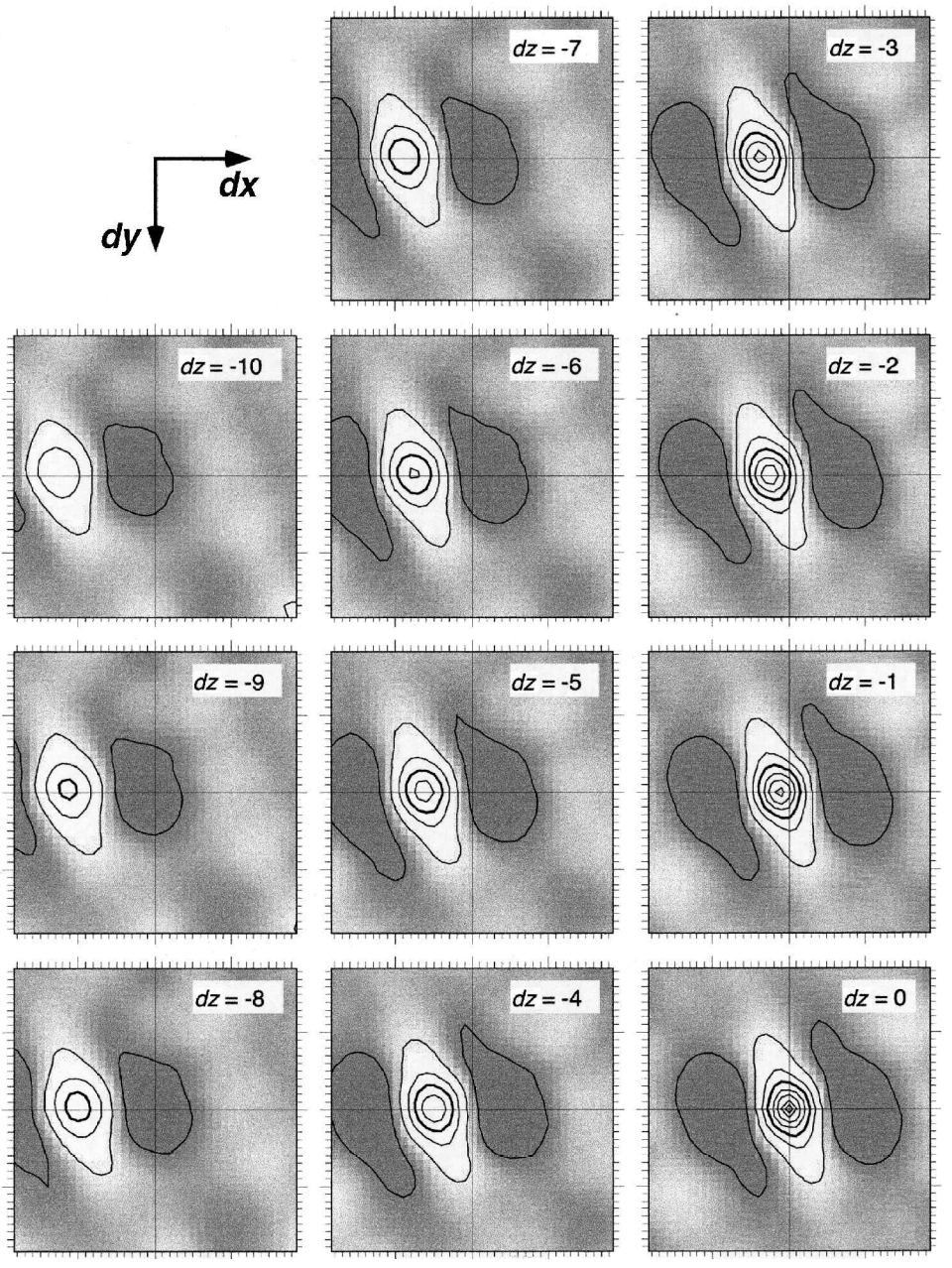

FIG. 8. Three-dimensional distribution of two-point correlation function $AC(dx, dy, dz)$ of the quartz rods. Each diagram shows a slice of $AC(dx, dy, dz)$ for fixed dz. The ranges of dx, dy and dz are $-18 \leqslant dx \leqslant +18$, $-18 \leqslant dy \leqslant +18$ and $-10 \leqslant dz \leqslant 0$, respectively, and the centre point of each diagram is $(dx, dy) = (0,0)$. Since the function is symmetrical with respect to the origin $(dx, dy, dz) = (0,0,0)$, the slices for $+1 \leqslant \mathrm{dz} \leqslant +10$ can be derived from the slices shown in the figure. Contour lines are drawn at an interval of 0.0232 which is 1/10 of $AC(0,0,0)$. The bold line indicates $AC(dx, dy, dz) = 0.116$ which is half of $AC(0,0,0)$.

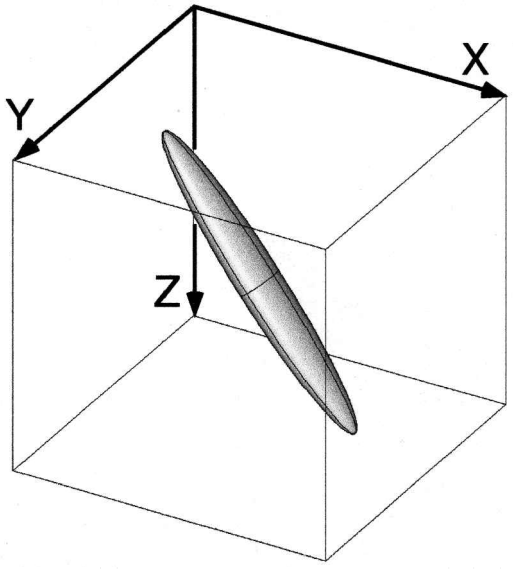

FIG. 9. The average three-dimensional shape of quartz rods in the specimen derived from an ellipsoid fitting to the high value area of two-point correlation function ($AC(dx, dy, dz) \geqslant 0.116$) shown in Fig. 8. The rectangular cell corresponds to that of Fig. 6*f*.

According to the crystallographic analysis by a precession camera, this elongation direction (i.e. *c*-axis of the fitted ellipsoid) corresponds approximately to the crystallographic *c*-axis of the quartz rods.

Such image analysis of crystallographic preferred orientation using the elongation axis has been carried out in only two dimensions (e.g. Simigian and Starkey, 1986). Thus this shape analysis by 2-point correlation function and ellipsoid fitting is useful not only for investigation of shape but also for the crystallographic orientation analysis in three dimensions.

Conclusions

We developed techniques to analyse 3-dimensional connection and the shapes of crystals by X-ray CT and image analysis. Graphic granite was the material selected for these analyses. The conclusions in this study are summarized as follows:

(1) The difference in CT values from one slice to another was recognized. This difference is due to the beam-hardening, and we corrected the CT values based on the cross-sectional areas of the specimen.

(2) The cluster labelling technique showed at least 89.9% of the quartz rods to be connected with each other in the specimen. This result of interconnection of quartz rods was consistent with the previous study by Simpson (1962).

(3) The 2-point correlation function was calculated in order to investigate the 3-dimensional shape of the quartz rods. The ellipsoid fitted to the high-value area of the function represented a very elongated shape whose elongation axis almost corresponded to the crystallographic *c*-axes of the quartz rods.

Furthermore, we confirmed the following useful points: (1) We can obtain quantitative information on the connection of crystals using the 'connectivity' value. (2) We can observe the precise structure of junctions of connected crystals from various angles by image processing. (3) We can obtain the average shape and elongation axis of crystals by 2-point correlation function and an ellipsoid fitting. (4) All of these processes can be performed 3-dimensionally and non-destructively. (5) The techniques are not time-consuming.

Acknowledgements

We would like to thank C. Matsue for sample preparation and M. Shimizu and Y. Yabe, who provided useful information on the geology of pegmatites in Ishikawa town. We are deeply indebted to T. Ozawa and M. Nespolo for their help in the determination of crystallographic orientations using a precession camera. The analysis with the precession camera was performed at the Mineralogical Institute, University of Tokyo. We are grateful to A. Tsuchiyama and T. Hanamoto for their kind suggestion with respect to the theory of X-ray absorption. Helpful advice from K. Nakamura, T. Ohtani, M. Toriumi, H. Nagahara, and T. Hiraga is gratefully acknowledged. Thanks are due to S. Sasaki for allowing us to use a personal computer (CD-R writing system). A review by an anonymous referee helped to improve the manuscript. This research was supported in part by a Research Fellowship of the Japan Society for the Promotion of Science for Young Scientists, and a Grant-in-Aid for Scientific Research from the Ministry of Education, Science and Culture, Japan (to S.I.) and by the grant from the Agency of Industrial Science and Technology (to Y.N.).

References

Berryman, J.G. (1985) Measurement of spatial correlation functions using image processing techniques. *J. Appl. Phys.*, **57**, 2374–84.

Berryman, J.G. and Blair, S.C. (1986) Use of digital image analysis to estimate fluid permeability of porous materials: Application of 2-point correlation functions. *J. Appl. Phys.*, **60**, 1930–8.

Bryon, D.N., Atherton, M.P. and Hunter, R.H. (1995) The interpretation of granitic textures from serial thin sectioning, image analysis and three-dimensional reconstruction. *Mineral. Mag.*, **59**, 203–11.

Cashman, K.V. and Marsh, B.D. (1988) Crystal size distribution (CSD) in rocks and the kinetics and dynamics of crystallization II: Makaopuhi lava lake. *Contrib. Mineral. Petrol.*, **99**, 292–305.

Cooper, M.R. and Hunter, R.H. (1995) Precision serial lapping, imaging and three-dimensional reconstruction of minus-cement and post-cementation intergranular pore-systems in the Penrith Sandstone of north-western England. *Mineral. Mag.*, **59**, 213–20.

Denison, C. and Carlson, W.D. (1997) Three-dimensional quantitative textural analysis of metamorphic rocks using high resolution computed X-ray tomography: Part II. Application to natural samples. *J. Metam. Geol.*, **15**, 45–57.

Denison, C., Carlson, W.D. and Ketcham, A. (1997) Three-dimensional quantitative textural analysis of metamorphic rocks using high-resolution computed X-ray tomography: Part I. Methods and techniques. *J. Metam. Geol.*, **15**, 29–44.

Dilks, A. and Graham, S.C. (1985) Quantitative mineralogical characterization by back-scattered electron image analysis. *J. Sed. Petrol.*, **55**, 347–55.

Fenn, P.M. (1986) On the origin of graphic granite. *Amer. Mineral.*, **71**, 325–30.

Hubbell, J.H., Gimm, H.A. and Øverbø, I. (1980) Pair, triplet and total atomic cross sections (and mass attenuation coefficients) for 1 MeV–100 GeV photons in elements z=1 to 100. *J. Phys. Chem. Ref. Data*, **9**, 1023–145.

Kawano, Y. and Ueda, Y. (1967) K-Ar dating on the igneous rocks in Japan (VI) – granitic rocks, summary. *J. Japan Assoc. Mineral. Petrol. Econ. Geol.*, **57**, 177–87 (Japanese with English abstract).

Koch, B. and MacGillavry, C.H. (1962) X-ray absorption. Pp. 157–60 in: *International Tables for X-ray Crystallography, Vol. III* (C.H. MacGillavry and G.D. Rieck, editors). The Kynoch Press, UK.

Lentz, D.R. and Fowler, A.D. (1992) A dynamic model for graphic quartz-feldspar intergrowths in granitic pegmatites in the southwestern Grenville Province. *Canad. Mineral.*, **30**, 571–85.

Marschallinger, R. (1998) Correction of geometric errors associated with the 3-D reconstruction of geological materials by precision serial lapping. *Mineral. Mag.*, **62**, 783–92.

Matsubara, H. (1956) Reports on the pegmatites in Ishikawa district, Fukushima Prefecture – One of the fundamental studies on uranium-thorium resources in Japan. *Bull. Geol. Surv. Japan*, **7**, 335–48 (Japanese with English abstract).

McCullough, E.C. (1975) Photon attenuation in computed tomography. *Medical Physics*, **2**, 307–20.

Morishita, R. (1998) Statistical properties of ideal rock textures: relationship between crystal size distribution and spatial correlation of minerals. *Math. Geol.*, **30**, 409–34.

Morishita, R. and Obata, M. (1995) A new statistical description of the spatial distribution of minerals in rocks. *J. Geol.*, **103**, 232–40.

Nakano, T. and Fujii, N. (1989a) Softwares for digital image processing: (1) painting and virtual screen management. *Geoinformatics*, **14A**, 93–107 (Japanese with English abstract).

Nakano, T. and Fujii, N. (1989b) The multiphase grain control percolation: its implication for a partially molten rock. *J. Geophys. Res.*, **94**, 15653–61.

Nakano, T. and Fujii, N. (1991) Softwares for digital image processing: (3) cluster labelling and perimeter extraction. *Geoinformatics*, **2**, 23–44 (Japanese with English abstract).

Nakano, T., Nishizawa, O., Masuda, K., Inazumi, T. and Kasama, S. (1992) Three-dimensional distribution of cracks and minerals in a rock obtained by X-ray CT. *Geotomography, SEGJ Int. Pub.*, **2**, 361–71.

Nakano, T., Nakamura, K., Someya, T. and Ohtsuka, H. (1997) Observation of 3-dimensional internal structure of rock using X-ray CT: (1) density calibration of CT value. *Geoinformatics*, **8**, 239–55 (Japanese with English abstract).

Nakashima, Y., Hirai, H., Koishikawa, A. and Ohtani, T. (1997) Three-dimensional imaging of arrays of fluid inclusions in fluorite by high-resolution X-ray CT. *Neues Jahrb. Mineral. Mh.*, 559–68.

Philpotts, A.R., Shi, J. and Brustman, C. (1998) Role of plagioclase crystal chains in the differentiation of partly crystallized basaltic magma. *Nature*, **395**, 343–6.

Raynaud, S., Fabre, D., Mazerolle, F., Geraud, Y. and Latiere, H. (1989) Analysis of the internal structure of rocks and characterization of mechanical deformation by a non-destructive method: X-ray tomodensitometry. *Tectonophysics*, **159**, 149–59.

Simigian, S. and Starkey, J. (1986) Automated grain shape analysis. *J. Struct. Geol.*, **8**, 589–92.

Simpson, D.R. (1962) Graphic granite from the Ramona pegmatite district, California. *Amer. Mineral.*, **47**, 1123–38.

Stauffer, D. (1985) *Introduction to Percolation Theory*. Taylor & Francis, Philadelphia, PA, USA.

Stel, H. (1992) Diagnostic microstructures for primary and deformational quartz rods in graphic granite. *Amer. Mineral.*, **77**, 329–35.

Wahlstrom, E.E. (1939) Graphic granite. *Amer. Mineral.*, **24**, 681–98.

[*Manuscript received 16 February 1999: revised 7 July 1999*]

Appendix

Ellipsoid-fitting to a three-dimensional object

We carried out ellipsoid-fitting to the 3-dimensional object (i.e. high-value region of a 2-point correlation function) and obtained the directions of principal axes and the ratios between the radii of the object (ellipsoid). This fitting was performed on the assumption that the centre of balance of the object corresponded with the centre of the ellipsoid. Firstly, the direction the *c*-axis of the ellipsoid was determined by minimizing the 2nd moment around *c*-axis. Next, the *a*-axis was determined by maximizing the 2nd moment around *a*-axis. The detailed calculation process is as follows.

Expression of an ellipsoid

Here we show the fundamental equations which express an ellipsoid. Internal space within an ellipsoid was expressed as:

$$\left(\frac{a}{A}\right)^2+\left(\frac{b}{B}\right)^2+\left(\frac{c}{C}\right)^2\leqslant 1 \qquad \text{(A1)}$$

where *a, b* and *c* indicate the values of a coordinate of the point in *abc*-coordinate system, and *A, B* and *C* indicate the radii on the *a, b* and *c*-axes, respectively (Fig. A1*a*). In this appendix we define $A\leqslant B\leqslant C$. The volume of the ellipsoid is expressed as:

$$V=\int\int\int dadbdc=\frac{4}{3}\pi ABC \qquad \text{(A2)}$$

The 2nd moment around the origin of the coordinate axes (*a, b* and *c*-axes) is expressed as:

$$\begin{aligned} M_0 &= \int\int\int (a^2+b^2+c^2)dadbdc \\ &= \frac{1}{5}V(A^2+B^2+C^2) \end{aligned} \qquad \text{(A3)}$$

The 2nd moments around the *a, b* and *c*-axes are expressed as:

$$\begin{aligned} \begin{Bmatrix} M_a \\ M_b \\ M_c \end{Bmatrix} &= \int\int\int \begin{Bmatrix} (b^2+c^2) \\ (c^2+a^2) \\ (a^2+b^2) \end{Bmatrix} dadbdc \\ &= \frac{1}{5}V \begin{Bmatrix} (B^2+C^2) \\ (C^2+A^2) \\ (A^2+B^2) \end{Bmatrix} \end{aligned} \qquad \text{(A4)}$$

Transformation between the coordinates

Here we show the way to transform a coordinate belonging to a coordinate system into a coordinate belonging to other coordinate systems. If the *abc*-coordinate system is not the same as the *xyz*-coordinate system, i.e. if the angles λ, ϕ and θ in Fig. A1*b* $\neq 0$, we have to transform the coordinates to express the ellipsoid in the *xyz*-coordinate system. The transformation of the coordinate belonging to the *abc*-coordinate system can be transformed into the coordinate belonging to the *xyz*-coordinate system by the equation

$$\begin{pmatrix} x \\ y \\ z \end{pmatrix} = a\vec{e}_a + b\vec{e}_b + c\vec{e}_c \qquad \text{(A5)}$$

where

$$\begin{aligned} \vec{e}_a &= \begin{pmatrix} \sin\lambda\cos\theta+\cos\lambda\sin\phi\sin\theta \\ -\cos\lambda\cos\theta+\sin\lambda\sin\phi\sin\theta \\ -\cos\phi\cos\theta \end{pmatrix}, \\ \vec{e}_b &= \begin{pmatrix} -\sin\lambda\sin\theta+\cos\lambda\sin\phi\cos\theta \\ \cos\lambda\sin\theta+\sin\lambda\sin\phi\cos\theta \\ -\cos\phi\cos\theta \end{pmatrix} \text{ and} \\ \vec{e}_c &= \begin{pmatrix} \cos\lambda\cos\phi \\ \sin\lambda\cos\phi \\ \sin\phi \end{pmatrix} \end{aligned} \qquad \text{(A6)}$$

for $-\pi\leqslant\lambda\leqslant\pi$, $-\frac{1}{2}\pi\leqslant\phi\leqslant\frac{1}{2}\pi$, $-\pi\leqslant\theta\leqslant\pi$.

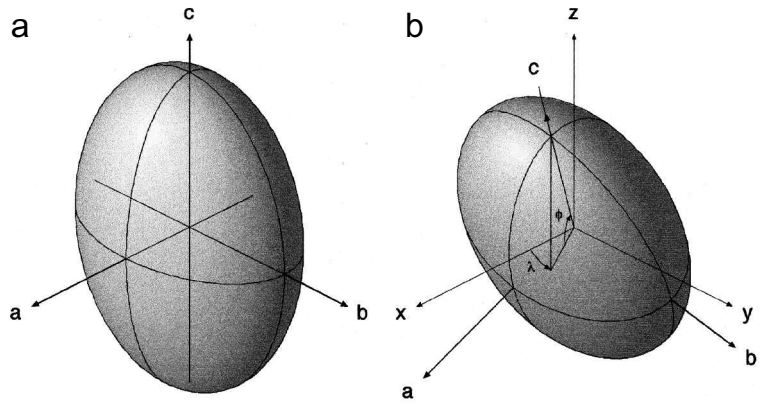

FIG. A1. Coordinate system expressing an ellipsoid. The sign of the *Z*-axis is reversed. (*a*) An ellipsoid and its principal axes. (*b*) The generalized coordinate system of ellipsoid in the case where the *abc*-axes of the ellipsoid do not correspond to the *XYZ*-axes of the observation coordinate system.

Image data

Image data are constructed in the *xyz*-coordinate system and the origin of the coordinate system does not lie at the centre of the object. Thus, as a simple calculation, we moved the origin of the coordinate system to the centre (of gravity) of the object. The centre of gravity of the object is expressed as a vector in the *xyz*-coordinate system:

$$\vec{\mathbf{R}}_0 = \frac{1}{N}\sum_{i=1}^{N}\begin{pmatrix} X_i \\ Y_i \\ Z_i \end{pmatrix} \qquad \text{(A7)}$$

where N is the number of voxels which belong to the object, and X, Y and Z are the values of the coordinate of the ith voxel. In the following calculations, this point (coordinate) is regarded as the centre of the *xyz*-coordinate system. Furthermore, the centre point of the ellipsoid was fixed at the origin of the *xyz*-coordinate system. Thus we transformed all the coordinates in the old *xyz*-coordinate system into the new coordinates as follows:

$$\vec{r}_i = \begin{pmatrix} x_i \\ y_i \\ z_i \end{pmatrix} = \begin{pmatrix} X_i \\ Y_i \\ Z_i \end{pmatrix} - \vec{\mathbf{R}}_0 \qquad \text{(A8)}$$

Using equation A6, we can transform the coordinate of each voxel in *xyz*-coordinate system into the coordinate in *abc*-coordinate system

$$\vec{\mathbf{r}}_i = a_i\vec{\mathbf{e}}_a + b_i\vec{\mathbf{e}}_b + c_i\vec{\mathbf{e}}_c \qquad \text{(A9)}$$

The volume of the object and the 2nd moment around the origin of the coordinate axes are expressed as;

$$V = N\Delta \qquad \text{(A10)}$$

$$M_0 = \sum_{i=1}^{N}(a_i^2 + b_i^2 + c_i^2)\Delta = \sum_{i=1}^{N}|\vec{\mathbf{r}}_i|^2\Delta = L_0\Delta \qquad \text{(A11)}$$

where Δ indicates the volume of each voxel and L_0 is

$$L_0 = \sum_{i=1}^{N}(x_i^2 + y_i^2 + z_i^2) \qquad \text{(A12)}$$

From equations A3, A10 and A11, we can obtain

$$A^2 + B^2 + C^2 = 5M_0/V = 5L_0/N \qquad \text{(A13)}$$

Determination of the c-axis

From the calculations above we established the essential values of the object. Here we determine the *c*-axis of the object. Only the angles λ and ϕ are involved in these calculations. The angle θ is

irrelevant. From equations A6, A8, A9, A10 and A11, the 2nd moment around the c-axis is expressed as:

$$\begin{aligned} M_c &= \sum_{i=1}^{N}(a_i^2+b_i^2)\Delta = \sum_{i=1}^{N}\left(|\vec{\mathbf{r}}_i|^2 - c_i^2\right)\Delta \\ &= M_0 - \sum_{i=1}^{N} c_i^2\Delta = M_0 - \sum_{i=1}^{N}(\vec{\mathbf{r}}_i\cdot\vec{\mathbf{e}}_c)^2\Delta \\ &= M_0 - \sum_{i=1}^{N}\{(x_i\cos\lambda + y_i\sin\lambda)\cos\phi + z_i\sin\phi\}^2\Delta \end{aligned} \tag{A14}$$

We determined λ and ϕ which minimizes the value of M_c. From equations A4 and A13, we can determine

$$A^2 + B^2 = 5M_c/N = 5L_c/N \tag{A15}$$

where

$$L_c = M_c/\Delta \tag{A16}$$

Finally, from equations A13 and A16, we can determine

$$C^2 = 5(L_0 - L_c)/N \tag{A17}$$

and then, we can determine the radius of C.

Determination of the a and b-axes

In the last section we determined the direction of the c-axis (i.e. the angles λ and ϕ) and radius C. In this section, we determine the angle θ by maximizing the 2nd moment around the a-axis. Maximizing the 2nd moment around the a-axis (M_a) is equivalent to minimizing the 2nd moment around the b-axis (M_b). Then we determine the radii B and C.

The 2nd moments around the a and b-axes are expressed as: (see equations A18 to 21 below)

$$\begin{aligned} M_a &= \sum_{i=1}^{N}(b_i^2+c_i^2)\Delta = \sum_{i=1}^{N}\left(|\vec{\mathbf{r}}_i|^2 - a_i^2\right)\Delta = M_0 - \sum_{i=1}^{N} a_i^2\Delta \\ &= M_0 - \sum_{i=1}^{N}(\vec{\mathbf{r}}_i\cdot\vec{\mathbf{e}}_a)^2\Delta = M_0 - \sum_{i=1}^{N}(h_i\cos\theta + \nu_i\sin\theta)^2\Delta \\ &= M_0 - L_{ab}(\theta)\Delta \end{aligned} \tag{A18}$$

$$\begin{aligned} M_b &= \sum_{i=1}^{N}(c_i^2+a_i^2)\Delta = \sum_{i=1}^{N}\left(|\vec{\mathbf{r}}_i|^2 - b_i^2\right)\Delta = M_0 - \sum_{i=1}^{N} b_i^2\Delta \\ &= M_0 - \sum_{i=1}^{N}(\vec{\mathbf{r}}_i\cdot\vec{\mathbf{e}}_b)^2\Delta = M_0 - \sum_{i=1}^{N}(-h_i\sin\theta + \nu_i\cos\theta)^2\Delta \\ &= M_0 - L_{ab}(\theta \pm \frac{1}{2}\pi)\Delta \end{aligned} \tag{A19}$$

where

$$L_{ab}(\theta) = \sum_{i=1}^{N}(h_i\cos\theta + \nu_i\sin\theta)^2 \tag{A20}$$

and

$$\begin{aligned} h_i &= x_i\sin\lambda - y_i\cos\lambda \\ \nu_i &= (x_i\cos\lambda + y_i\sin\lambda)\sin\phi - z_i\cos\phi \\ &(i = 1, \cdots, N) \end{aligned} \tag{A21}$$

We determined θ ($0 \leqslant \theta < \pi$) which minimizes the value of L_{ab}. Then we calculated

$$L_a = M_a/\Delta = L_0 - L_{ab}(\theta)$$
$$L_b = M_b/\Delta = L_0 - L_{ab}(\theta \pm \frac{1}{2}\pi) \qquad \text{(A22)}$$

From equations A4 and A13, we can obtain

$$B^2 + C^2 = 5M_a/V = 5L_a/N$$
$$C^2 + A^2 = 5M_b/V = 5L_b/N \qquad \text{(A23)}$$

Finally, from equations A13 and A16, we can obtain:

$$A^2 = 5(L_0 - L_a)/N$$
$$B^2 = 5(L_0 - L_b)/N \qquad \text{(A24)}$$

and then, we can determine the radii A and B.